J. Am. Soc. Mass Spectrom. (2018) 29:2160–2172
DOI: 10.1007/s13361-018-2038-3

RESEARCH ARTICLE

The FUNPET—a New Hybrid Ion Funnel-Ion Carpet Atmospheric Pressure Interface for the Simultaneous Transmission of a Broad Mass Range

Benjamin E. Draper, Staci N. Anthony, Martin F. Jarrold

Chemistry Department, Indiana University, Bloomington, IN 47405, USA

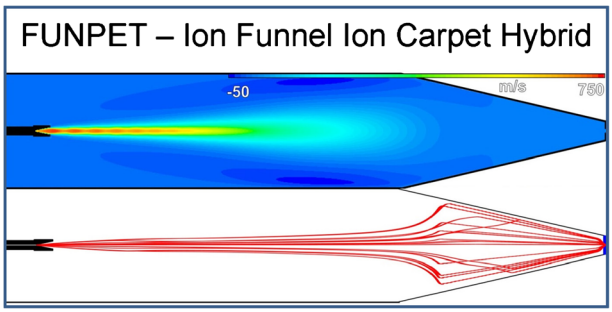

Abstract. An atmospheric pressure interface transports ions from ambient pressure to the low-pressure environment of a mass spectrometer. A capillary coupled to an ion funnel is widely used. However, conventional ion funnels do little to negate the large amount of energy picked up by high-mass ions from the gas flow through the capillary. There has been little work done on the effects of gas flow on ion transmission, and the previous studies have all been limited to low-mass, low-charge ions. In this work, we account for the effects of gas flow, diffusion, and electric fields (static and oscillating) on ion trajectories and use simulations to design a new hybrid ion funnel-ion carpet (FUNPET) interface that transmits a broad mass range with a single set of instrument conditions. The design incorporates a virtual jet disruptor where pressure buildup and counter flow dissipate the supersonic jet that results from gas flow into the interface. This, and the small exit aperture that can be used with the FUNPET, reduces the gas flow into the next stage of differential pumping. The virtual jet disruptor thermalizes ions with a broad range of masses (1 kDa to 1 GDa), and once thermalized, they are transmitted into next region of the mass spectrometer with low excess kinetic energy. The FUNPET interface is easy to fabricate from flexible printed circuit board and a support frame made by 3D printing. The performance of the interface was evaluated using charge detection mass spectrometry.

Keywords: Electrospray interface, Ion funnel, Ion carpet

Received: 26 May 2018/Revised: 14 July 2018/Accepted: 16 July 2018/Published Online: 15 August 2018

Introduction

There is increasing interest in using mass spectrometry to analyze ions in the megadalton regime, such as large protein complexes and viruses [1–3]. Electrospray is usually the preferred ionization method for these species as it can sample ions directly from solution. Electrospray is an ambient ionization technique, so an interface is required to transfer ions from ambient pressure to the high vacuum environment required for mass spectrometry measurements. The large pressure difference between atmospheric pressure and the first region of the mass spectrometer (which is typically at several hundred Pa) creates a directed gas flow that transports ions into the instrument. However, upon entering the first region of the mass spectrometer, the directed gas flow forms a supersonic jet that accelerates the ions transported in the flow to supersonic velocities [4]. A wide distribution of ion energies is undesirable because it is difficult to focus the ions, lowering transmission. Therefore, the usual approach is to thermalize them so that they can be accelerated to a known energy. The ideal interface must efficiently transmit all ions of interest, while being simple to build, use, and maintain. The two most common interfaces used in mass spectrometry are the ion funnel and the ion carpet [5–7].

The ion funnel was developed by Smith and coworkers in the 1990s and has been continually improved upon since [5, 8].

Electronic supplementary material The online version of this article (https://doi.org/10.1007/s13361-018-2038-3) contains supplementary material, which is available to authorized users.

Correspondence to: Martin Jarrold; *e-mail:* mfj@iu.edu

Broadly speaking, the ion funnel consists of a series of closely spaced ring electrodes with some having a constant inner diameter before tapering down to a small aperture. This aperture must be quite small, on the order of 1 mm, to reduce the gas load on subsequent regions of the instrument. The ion funnel confines and directs ions towards the exit aperture using both RF and DC potentials. RF signals, 180° out of phase, are applied to adjacent electrodes to confine the ions, with a DC drift field superimposed to drive ions towards the exit aperture. However, when the aperture diameter and the electrode spacing are comparable, the RF field creates axial wells that can trap ions and prevent them from being transmitted [9]. To mitigate this effect, the size of the aperture can be increased, the electrode spacing can be decreased, or the RF potentials can be removed from the final electrodes. However, increasing the aperture size increases the gas load on subsequent regions of the instrument, decreasing the electrode spacing increases the complexity and capacitance (increasing power requirements), and removing RF from the final electrodes reduces confinement and contributes to ion loss.

A notable improvement to the ion funnel was the addition of a jet disruptor, which is a small electrode placed directly in the path of the capillary jet. The jet disruptor is supplied with a DC potential that is slightly larger than the DC on the surrounding funnel electrodes. The jet disruptor acts as a physical barrier to the capillary jet, and the small DC voltage deflects ions around it so that they can be refocused by the ion funnel and transmitted. The jet disruptor reduces the gas load on subsequent regions of the mass spectrometer while maintaining high ion transmission [10, 11]. Another notable improvement came from Tridas and coworkers, who constructed a funnel using a flexible printed circuit board (PCB) housed in a scaffold produced by 3D printing. This greatly simplified the construction process and reduced both the capacitance and the cost [12].

An alternative interface, the ion carpet, was developed by Wada and coworkers in 2003 [6]. The ion carpet, or RF carpet, is essentially a compressed ion funnel; it consists of a series of concentric ring electrodes on a rigid PCB with a small aperture drilled through the center. Similar to the ion funnel, RF voltages are applied 180° out of phase to adjacent electrodes, with a DC drift field superimposed to drive ions into the exit aperture [6, 13]. The ion carpet can also provide high ion transmission in a DC-only mode [7]. The ion carpet is usually coupled with a separate drift region to thermalize ions before they reach the ion carpet. One advantage of the ion carpet is that a long drift region can be decoupled from the focusing field, and so a simple drift region with widely spaced ring electrodes can be used. This greatly reduces the capacitance of the overall device and simplifies the construction and maintenance of the interface [7].

Ion trajectory simulations are typically performed to model a mass spectrometer interface before construction. The most widely used program for these simulations is SIMION [14]. In addition to modeling the electric fields that are created in a user-generated device, additional programs have been written and incorporated to allow the inclusion of gas flow effects and to model diffusion. However, the statistical diffusion simulation (SDS) model used for intermediate pressures is limited to modeling ion sizes up to 10,000 times the mass of the background gas [15]. This mass restriction limits the program to modeling ion masses of approximately 300 kDa, when the background gas is air, and thus, it is not appropriate for modeling the very large biomolecules of interest here.

Other custom ion trajectory codes that have been written to model interfaces use an ion mobility model with both fast adjusting and pseudopotential RF fields [7, 16, 17]. However, the ion mobility model with fast adjusting RF fields also breaks down at large ion masses [5], and the pseudopotential approach does not accurately model low RF frequencies. This is because the pseudopotential is inversely proportional to the square of the frequency, and thus, lower frequencies only increase the strength of the pseudopotential, which would increase confinement in, say, a series of ring electrodes. However, it is possible for the frequency to oscillate too slowly to properly confine ions, and the pseudopotential model does not reflect this.

Most trajectory simulations of ion funnel interfaces have been limited to a static background gas. The simulations ignore the directed gas flow that is known to result from the large pressure difference across the capillary. There have been several recent efforts to understand how ion trajectories are affected by gas flow; however, this work has focused on low-mass and low-charge ions [11, 18–23]. Large ions have large collision cross sections and so they are more susceptible to the influence of gas flow [24].

There are two main methods for simulating gas flow, the choice depending on the gas density. For high-density flows, the continuum assumption is appropriate because the microscopic fluctuations in the fluid density are small compared to the length scale of the region being simulated. Continuum gas flow is well characterized by numerical solutions to the Navier-Stokes equation [25]. The continuum assumption fails for low-density flows where local fluctuations are significant such that the gas must be treated as individual particles. These flows are characterized by probabilistic solutions to the Boltzmann equation using the direct simulation Monte Carlo method (DSMC) developed by Bird [26]. Mass spectrometer interfaces often have intermediate densities that fall within the transitional flow regime. The best solver for this regime can vary depending on pumping and interface geometry.

With the increasing interest in mass spectrometry measurements for large ions, it is important to characterize and optimize interfaces for them. In this work, we simulate the motion of kilodalton- to gigadalton-sized ions in a flowing gas for the first time and use these findings to design an interface that maximizes transmission and minimizes excess kinetic energy for a broad mass range. To simulate ion motion, a new ion trajectory program was written using the velocity Verlet algorithm with Langevin dynamics. It incorporates electric fields from SIMION 8.1, drag from gas flow information, diffusion, and gravity. We examined a variety of interfaces and eventually settled on a hybrid interface that incorporates favorable aspects of both an ion funnel and an ion carpet. This new ion funnel-ion carpet hybrid is termed a FUNPET.

Computational Methods

We start by describing the four interfaces considered in this study. In all of the interfaces, the ions and gas enter the first differentially pumped region through a heated metal capillary (10-cm long, 0.381-mm ID). Trajectory simulations start after the ions have passed through the capillary, and it is assumed that the ions have the same initial velocity as the background gas at that point.

Interface 1: Open Drift Region with an Ion Carpet and Physical Jet Disruptor

In this interface, the drift region is composed of 74 ring electrodes with a constant inner diameter of 2.54 cm. The electrodes are 0.508 mm thick with 3.81 mm spacing between them, for a total length of 31.57 cm. RF signals, 300 V peak to peak (V_{pp}) and 180° out of phase, are applied to adjacent electrodes. A constant drift gradient of 5 V/cm is also applied. A 6.35-mm diameter jet disruptor is placed halfway down the length of the drift region. The ion carpet is placed 6.35 mm from the end of the drift region. The carpet is composed of 24 concentric ring electrodes 0.254 mm high, 0.381 mm wide, and spaced by 0.127 mm. The exit aperture in the center of the ion carpet is 1.016-mm diameter and 1.016-mm long. A non-linear DC voltage gradient is applied to the ion carpet, with the innermost electrode grounded and the outer three electrodes held at 274 V. The voltage gradient is steeper near the exit aperture. No RF is applied to the ion carpet.

Interface 2: Sealed Drift Region with Ion Carpet and No Physical Jet Disruptor

In this interface, the layout of the drift region and ion carpet is identical to interface 1 above but with the gaps between the electrodes sealed by an insulator. In addition, the physical jet disruptor has been removed. A non-linear voltage gradient is applied to the drift region, with the first 15.5 cm having 40 V/cm, the last 11 cm having 0.5 V/cm gradient, and the middle 5 cm decreasing linearly from 40 to 0.5 V/cm. In addition, the voltage gradient applied to the ion carpet is 10% of the gradient used above for interface 1. Finally, to reduce the radial expansion of the jet, a 1-cm long diverging nozzle (0.75-mm ID to 5-mm ID) was added to the end of the capillary inlet. Diverging nozzles are known to increase the centerline intensity [27–29]. The end of the nozzle protrudes 2 cm into the drift region.

Interface 3: Sealed Ion Funnel with Virtual Jet Disruptor

The third interface is an ion funnel composed of a series of square ring electrodes, as it was anticipated that this interface would be made out of eight rigid PCBs: four rectangular boards for the straight drift region and four triangular boards for the funnel region. The square ring electrodes are 0.635 mm wide with 0.635 mm spacing between adjacent electrodes, for a total electrode pitch of 1.27 mm. The straight drift region is composed of 204 electrodes, for a total length of 26 cm, with an inner diameter of 7.62 cm. The final 104 electrodes taper down to a 2-mm inner diameter exit aperture, for a full funnel length of 42 cm. RF signals, 300 V peak to peak (V_{pp}) and 180° out of phase, are applied to adjacent electrodes, as with interfaces 1 and 2 above. However, the final four electrodes are not supplied with RF. A constant drift gradient of 5 V/cm is applied across the entire funnel. Finally, the diverging nozzle inlet protrudes 3 cm into the ion funnel.

Interface 4: FUNPET with Virtual Jet Disruptor

The fourth interface is a combination of the sealed drift region-ion carpet and ion funnel interfaces. A circular funnel with a 2.54-mm electrode pitch tapers down to a 6.35-mm inner diameter, with a 6.35-mm diameter ion carpet placed 1.27 mm from the last electrode of the ion funnel. A 300 V_{pp} RF signal is applied, though now all funnel electrodes are supplied with RF. A non-linear drift gradient is again used, where the first 30.5 cm has a gradient of 5 V/cm; the final 5 cm has a gradient of 1 V/cm, and the intervening 4 cm has a gradient that decreases linearly from 5 to 1 V/cm. In addition, the ion carpet has a voltage gradient that is 4% of the value used in interface 1—just 12 V across the entire structure. As in the previous ion funnel simulation, the capillary-diverging nozzle inlet protrudes 3 cm into the interface.

Gas Flow Simulations

The characterization of the gas entering the interface began with understanding the gas flow through the heated metal capillary. Due to the large pressure difference across the capillary, it was expected that the flow exiting the capillary would form a supersonic jet [4]. The capillary (10-cm long, 0.381-mm ID) was the same for all four interfaces. The volume flow through the capillary was calculated using the Wutz/Adams turbulent model which has been shown to agree well with experiments if the capillary length to internal diameter (ID) ratio is sufficiently large (> 50) [30]. Gas flow simulations were performed to understand the properties of the capillary jet and how it is affected by the interface. The results from the gas flow simulations were then imported into the ion trajectory program to understand the effect of gas flow on both ion transmission and the ions' excess kinetic energy. Two methods were used to model gas flow, the choice depending on the gas density.

The low background pressure (93 Pa) of the open drift region of interface 1 was best suited to analysis by the DSMC program, DS2V, though the inlet pressure was too high to be modeled directly. To make the inlet conditions accessible to the DS2V program, modeling of the entering gas flow started after its initial expansion from the capillary. The entrance boundary was set at the background pressure and the diameter of the calculated barrel shock for the jet expansion. All simulations of the open drift region used a 2D axisymmetric model of the

region, where the gas was treated as hard spheres with diffuse reflection from all surfaces. The initial state of the system was vacuum, and exit boundaries were set at the carpet aperture and the pumping location downstream from the capillary. The DS2V simulation of the open drift region of interface 1 was run until the flow reached a steady state.

The DSMC method was originally tried with the closed drift region (interfaces 2–4), but the pressure buildup that occurred led to unmanageable simulation times. For efficiency, and to more accurately model the higher density gas in the closed interface designs, it was necessary to use a continuum-based solver. In this work, Star-CCM+ v10.06 (CD-Adapco) was used for all closed interface simulations. Solver settings were chosen for compressible flow of an ideal gas [25]. Pressure outlets were set for the region behind the capillary (93 Pa) and at the exit aperture (10 Pa) of each interface design. The initial pressure inside the closed drift region was set at 93 Pa (based on the measured pressure for a similar configuration in previous instruments) [7]. Convergence was judged to have occurred when the exit mass flow rate equaled the entrance mass flow rate (± 5%).

Diffusion

Diffusion was incorporated with the Langevin dynamics model [31], as adapted by Crooks and coworkers into a velocity Verlet algorithm [32]. Langevin dynamics adds two additional force terms to Newton's second law of motion to account for a particle's dampened motion due to friction (i.e., drag) and a random force representing stochastic collisions with a fictitious background gas (i.e., diffusion). In this work, the diffusion coefficient was calculated with the Einstein relation, and the ion's mobility was calculated with the Mason-Schamp equation [33, 34]. The seven-step velocity Verlet algorithm developed by Crooks and coworkers is given by [32]

$$v\left(n+\frac{1}{4}\right) = \sqrt{a}\, v(n) + \sqrt{\frac{1-a}{\beta m}}\, N^{+}(n) \tag{1}$$

$$v\left(n+\frac{1}{2}\right) = v\left(n+\frac{1}{4}\right) + \frac{b\Delta t}{2}\,\frac{f(n)}{m} \tag{2}$$

$$r\left(n+\frac{1}{2}\right) = r(n) + \frac{b\Delta t}{2}\, v\left(n+\frac{1}{2}\right) \tag{3}$$

$$H(n) \rightarrow H(n+1) \tag{4}$$

$$r(n+1) = r\left(n+\frac{1}{2}\right) + \frac{b\Delta t}{2}\, v\left(n+\frac{1}{2}\right) \tag{5}$$

$$v\left(n+\frac{3}{4}\right) = v\left(n+\frac{1}{2}\right) + \frac{b\Delta t}{2}\,\frac{f(n+1)}{m} \tag{6}$$

$$v(n+1) = \sqrt{a}\, v\left(n+\frac{3}{4}\right) + \sqrt{\frac{1-a}{\beta m}}\, N^{-}(n+1) \tag{7}$$

The variables r and v are the particle's position and velocity, n is the current time, Δt is the time step, f represents the drag force acting on the particle, m is the particle mass, β is the inverse of k_BT (where k_B is Boltzmann's constant and T is temperature), and a represents the dampened velocity due to drag. N^{+} and N^{-} are independent, standard normal deviates that are used to model the stochastic motion of the particle. The variable b is a scaling factor used to ensure the accuracy. Step 4 is an explicit Hamiltonian update. For the work presented herein, the Hamiltonian update step was omitted, and the scaling factor was determined to be unnecessary due to the small time step employed in the simulation. In addition, the dampened velocity term was omitted in favor of incorporating the drag force (see below) directly into the force term present in steps 2 and 6. This is because the dampened velocity term assumes a static background gas, whereas our drag model incorporates a flowing background gas. Simulations demonstrated good agreement between the two drag models.

This model was tested against a simple Monte Carlo diffusion simulation to determine its accuracy. The final positions of a large group of diffusing particles for a large number of time steps were recorded, and the distributions were compared. At long time scales, large ion mass, and high background pressure, both models gave the expected Gaussian distribution of final positions. At short time scales, small ion mass, and low pressure, the Langevin dynamics model deviated from the Gaussian distribution generated by the Monte Carlo method. However, this is to be expected, as a large number of collisions are needed to create a Gaussian distribution of final positions, and shorter time, lighter mass, and lower pressure all result in fewer collisions. The diffusion model was therefore deemed appropriate.

Ion Trajectory Simulations

The ion trajectory simulations were performed using a velocity Verlet algorithm that incorporated a Langevin dynamics diffusion model, gas flow information through a drag model, forces from electric fields from SIMION 8.1, and gravity. This was all incorporated into a custom Fortran program written using OpenMP directives so that thousands of ions could be analyzed in a timely manner. In addition to determining the fraction of incident ions that are transmitted, the ion energy is tracked to ensure that the ions are thermalized. A flow diagram of the algorithm used to perform the ion trajectory simulations is shown in Supplementary Figure S1. While we account for all factors that influence the motion of individual ions in an electrospray interface, we do not account for space charge

effects that result from ion-ion interactions. These multibody interactions are difficult to incorporate. They depend on the ion density and ultimately limit the maximum ion current that can be transmitted by the interface.

The first step is to write and refine a SIMION geometry file. DC and RF potentials were applied to all electrodes, and potential array files were printed out. Local gas pressure and velocity information are extracted from the DS2V or Star-CCM+ simulations, and a lookup table was created. The trajectory calculation begins by initializing the ion's position. For interfaces with a diverging nozzle, all ions start at the same axial position, with a random radial position. The ion's initial velocity is set equal to that of the surrounding gas flow, as we expect that all ions will be moving with the gas flow towards the end of the capillary. Once the ion position and velocity have been set, the trajectory simulation begins.

At each time step, a bilinear interpolation for the gas flow values and a trilinear interpolation for the electric field values are performed for the ion's location. The ion's velocity is calculated relative to that of the surrounding gas flow; this relative velocity and the pressure of the surrounding gas are used to calculate a drag force, which is converted to an acceleration using the ion's mass. The acceleration due to the electric fields is then calculated. The total acceleration is determined by summing the contributions from drag, the electric fields, and gravity. The diffusion constant is determined from the local pressure and incorporated into the diffusion model, and a position and velocity update due to the diffusion is obtained. The ion's position is then updated based on its current velocity, the total acceleration due to the electric fields, drag, gravity, and diffusion. The ion velocity is then updated in a similar manner, the total velocity is calculated, and the ion energy is determined. The program then records the ion's position and energy and checks to see if the ion has crashed out on an electrode and if not, the cycle is repeated. Once all ions have either crashed out or been transmitted, the percent transmission and the mean and standard deviation of the final energy are calculated for each ion mass studied.

Results

For each interface, simulations were performed for masses ranging from 1 kDa to 1 GDa, with 1000 ions for each mass. The ions were assumed to be spherical, with a density equal to the density of water, and the charge was calculated using the Rayleigh limit [35]. While near-spherical ions typically charge to only 60–80% of the Rayleigh limit when electrosprayed, non-spherical ions usually receive a higher charge. The RF frequency was tuned to maximize transmission for each interface and for each *m*/*z*.

Interface 1: Open Drift Region with an Ion Carpet and Physical Jet Disruptor

The low pressure in the open drift region is suitable for DSMC simulations. The axial velocity from the DS2V simulation (Figure 1a) shows that the jet disruptor does mostly stop the jet. Some gas flows around the jet disruptor where it then recombines and flows towards the pumping and carpet apertures located at the end of the drift region. This appears to contradict the observations of Tridas and coworkers, who reported that gas did not flow around the jet disruptor [11]. However, the pressure is lower here, allowing a larger radial expansion of the jet. The radial velocity (Figure 1b) shows a large value just before the jet disruptor and then a negative value as the flow recombines after the jet disruptor. Also, note the positive radial velocity at the carpet wall showing that the gas flow is colliding with the wall. The local pressure (Figure 1c) shows that most of the drift region is centered around the expected 93 Pa, with the exception of the area immediately before the jet disruptor.

Ion trajectories for this interface are shown in Figure 1d–f. Twenty representative trajectories are shown for 1 kDa (Figure 1d), 1 MDa (Figure 1e), and 1 GDa (Figure 1f). The 1-kDa ions travel around the jet disruptor; they are refocused to the central axis by the gas flow and then focused by the ion carpet at the end. As the mass increases, the ions are no longer thermalized and they are lost on the surface of the jet disruptor. The diffusion coefficient is inversely proportional to the mass, so the effect of diffusion is more apparent for smaller ions than the larger ones.

A summary of the ion trajectory simulations is shown in Figure 2. Figure 2a shows the ion transmission results. High transmission (> 85%) is achieved with interface 1 for only the two lightest ions, 1 and 10 kDa. Transmission is slightly higher

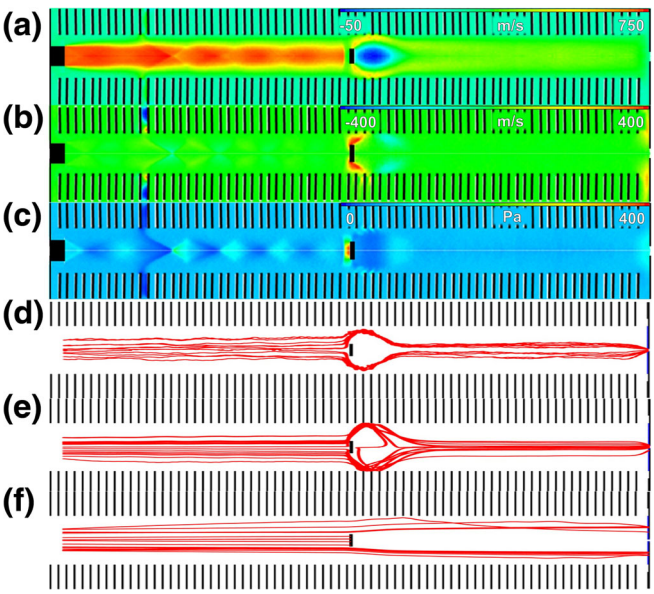

Figure 1. Gas flow and trajectories for interface 1: open drift region with an ion carpet and physical jet disruptor. Gas flow simulations performed using the DSMC solver DS2V. (**a**) Axial velocity, (**b**) radial velocity, and (**c**) pressure. Twenty representative ion trajectories of 1000 performed for each mass are shown for (**d**) 1 kDa, (**e**) 1 MDa, and (**f**) 1 GDa. The black vertical lines are the drift region electrodes, and the blue vertical line on the right-hand side is the ion carpet. The central black vertical line is the jet disruptor

for the 10-kDa ions because they are more strongly influenced by the gas flow and the gas flow after the jet disruptor returns them closer to the axis. Transmission drops for the heavier ions as they are too energetic to be deflected around the jet disruptor. Most of the 10-MDa ions crash out on the surface of the jet disruptor, and almost all of the larger ions suffer the same fate.

Figure 2b shows the average excess kinetic energy of the transmitted ions as a function of ion mass for all four interfaces studied. Supplementary Figure S2 shows a similar plot of excess kinetic energy but in units of eV/z. In both cases, the uncertainties (± 1 standard deviation) are smaller than the points. Due to the large electric field required on the carpet to focus the ions, the average excess kinetic energy of the ions that exit is quite high. The lightest ions pick up over 35 eV (15 eV/z) from the ion carpet. The largest ions that exit leave with nearly 1 MeV (363 eV/z). As mentioned previously, this broad distribution of ion energies is undesirable. However, the most important conclusion from these simulations is that the jet disruptor is ineffective for large ions because they collide with it. Therefore, an alternative, non-physical method of terminating the gas jet is necessary to ensure high transmission of all ion masses of interest.

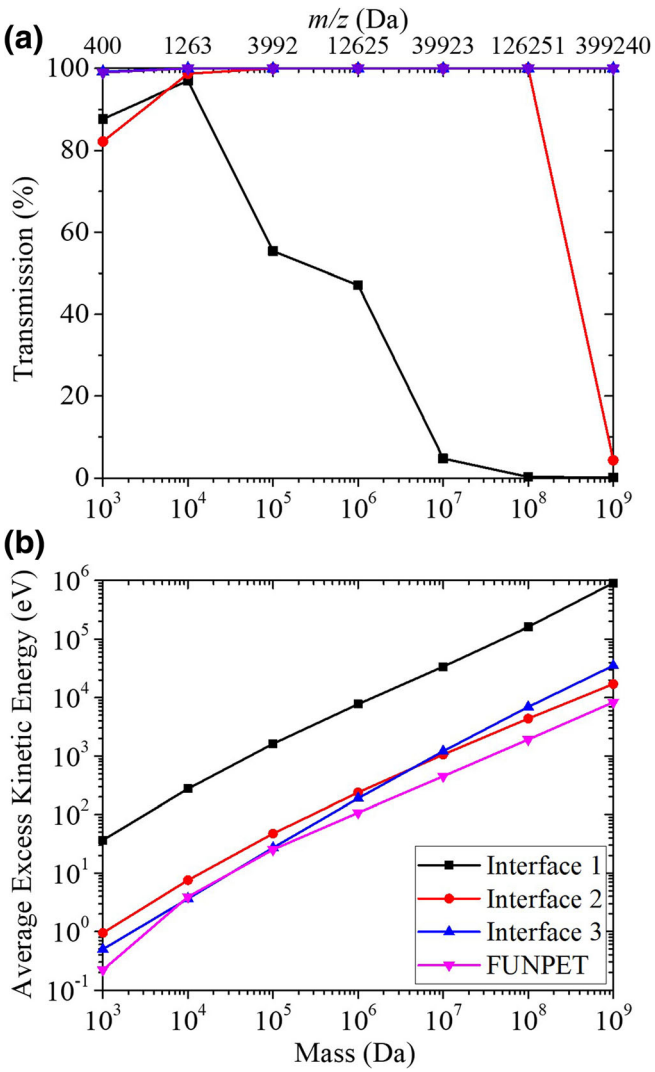

Figure 2. Plots of percent transmission and average excess kinetic energy as a function of ion mass (from 1 kDa to 1 GDa) for all four interfaces investigated. (**a**) Percent transmission through the exit aperture. (**b**) Average excess kinetic energy for the transmitted ions. The FUNPET (purple points and line) has the highest ion transmission and lowest excess kinetic energy

Interface 2: Sealed Drift Region with Ion Carpet and No Physical Jet Disruptor

Since a physical jet disruptor failed for high-mass ions, we sought to harness the gas flow itself as a virtual jet disruptor. We surmised that by sealing the drift region, there would be a pressure buildup at the carpet end of the drift region, and the counter flow of gas out of the drift region would help to dissipate the jet and thermalize the ions. Interface 2 was the first to incorporate these ideas. By sealing the drift region, the local pressure was expected to rise enough that the continuum assumption is appropriate for gas flow calculations. A diverging nozzle was used to reduce the radial expansion of the jet.

The axial velocity for the closed drift region (Figure 3a) shows that the jet is stopped ~ 15 cm from the capillary inlet. The local pressure at the carpet end rises to around 280 Pa (see Figure 3c), and the counter flow of gas around the jet is evident in Figure 3a. It is the combination of the counter flow and the pressure buildup at the carpet end of the drift region that provides the virtual jet disruptor that breaks up the jet and allows the ions to be thermalized. The performance of the virtual jet disruptor is enhanced by keeping the diameter of the drift region relatively small. Without the physical jet disruptor, the radial velocity (Figure 3b) is significantly less than with interface 1. The only notable radial velocity features

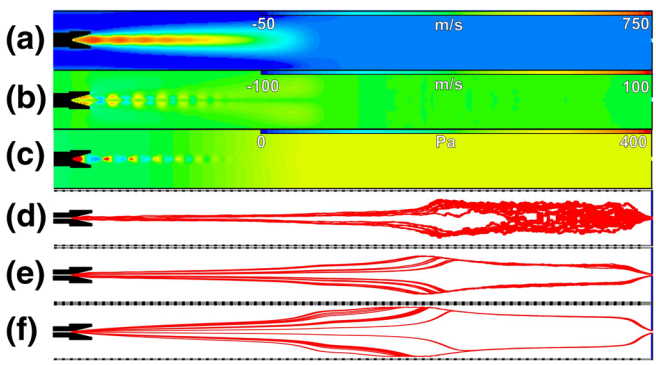

Figure 3. Gas flow and trajectories for interface 2: sealed drift region with ion carpet and no physical jet disruptor. Gas flow simulations performed using the Navier-Stokes solver Star-CCM+. (**a**) Axial velocity, (**b**) radial velocity, and (**c**) pressure. Twenty representative ion trajectories of 1000 performed for each mass are shown for (**d**) 1 kDa, (**e**) 1 MDa, and (**f**) 1 GDa. The black structure on the left is the end of the capillary-diverging nozzle inlet. The thick gray bar along the inner portion of the drift region electrodes indicates that the gaps between the electrodes have been closed. The blue lines on the far right represent the ion carpet

are the expansion and compression of the under-expanded jet exiting the diverging nozzle [4].

A disadvantage of the pressure buildup at the carpet end of the drift tube is that it increases the gas load on subsequent regions of the mass spectrometer. Because of the pressure buildup, it was necessary to increase the drift gradient on the first 15 cm of the drift region to 40 V/cm. Increasing the drift field reduced the time that the ions have to diffuse, preventing them from getting caught in the counter flow and lost. At the carpet end of the drift region, the gas is near-static and the drift field was reduced to 0.5 V/cm. The voltage gradient on the ion carpet was reduced to 10% of the gradient in interface 1. Lowering these voltage gradients should reduce the ions' excess kinetic energy.

Figure 3d–f shows sample trajectories for 1-kDa, 1-MDa, and 1-GDa ions. For all ion masses, a radial expansion occurs in the latter portion of the drift region due to the change in the potential gradient (it becomes weaker at the carpet end and so there is a field component orthogonal to the axis) and the gas flow (where a small radial component results because the flow is transitioning from axial flow towards the carpet to counter flow along the edge of the drift region).

The transmission for interface 2 is close to 100% for all ion masses between 10 kDa and 100 MDa (see Figure 2a), a dramatic improvement over interface 1. With the reduced drift field at the carpet end of the drift region in interface 2, and the absence of a significant gas flow, diffusion plays a much greater role, particularly for the small, low-mass ions. Diffusion causes some of the ions to be lost on the surface of the carpet. This is responsible for the reduced transmission efficiency of the 1-kDa ions (see Figure 2a). This was confirmed by re-running the ion trajectory simulations for the 1-kDa ions without diffusion, and 100% transmission was achieved. However, diffusion is not responsible for the poor transmission efficiency of the 1-GDa ions. Here, the issue is their large radial expansion and the difficulty of focusing them with the ion carpet.

In addition to the greatly improved ion transmission, the ions' average excess kinetic energy is much improved. The excess kinetic energy dropped by a factor of ~ 35 for all masses (see Figure 2b). However, the kinetic energy of the few transmitted 1-GDa ions still exceeds 10 keV, and lowering any of the voltage gradients only further reduces transmission. While much improved, the average ion energy is still higher than desired.

The main problem with interface 2 is the low transmission of high-mass ions which results because the carpet is not very effective at focusing ions that are a long way off-axis. In an effort to address this problem, we decided to revisit the ion funnel interface. The ion funnel has a longer focusing region than the carpet, which should help to transmit ions that travel a long way off-axis. However, interface 3 will employ a virtual jet disruptor instead of a physical one. Thus, the ion funnel should have a relatively long and narrow drift region that is sealed so that a virtual jet disruptor can be generated by the gas pressure buildup and counter flow.

Interface 3: Sealed Ion Funnel with Virtual Jet Disruptor

It is desirable to reduce the gas flow from the interface into subsequent regions of the mass spectrometer, and so we increased the inner diameter compared to interfaces 1 and 2. With the increased diameter, the jet took longer to dissipate and so we extended the length of the drift region as well.

The gas flow axial velocity (Figure 4a) for the ion funnel shows the jet stopped ~ 27 cm away from the capillary inlet (around twice as far as in interface 2). The radial velocity (Figure 4b) shows the same radial velocity features as seen for interface 2 (resulting from expansion and compression of the under-expanded jet). The pressure buildup near the exit of the funnel is close to 195 Pa (compared to 280 Pa with interface 2) (see Figure 4c). The lower pressure buildup is due to the larger diameter and this leads to the longer jet stopping distance noted above.

The combination of the small aperture (1-mm diameter) and RF field creates axial wells that trapped the small ions and lowered transmission. It was therefore necessary to both increase the aperture to a 2-mm diameter and remove the RF potential from the last four funnel electrodes to allow all ions to be transmitted. The decreased pressure in the ion funnel should reduce the gas load on the next region; however, the 2-mm ID aperture results in a mass flow rate out the exit aperture (1.48×10^{-7} kg/s) greater than that of the higher pressure drift region in interface 2 (6.68×10^{-8} kg/s). Because of the larger inner diameter, it was possible to use a constant 5-V/cm drift gradient

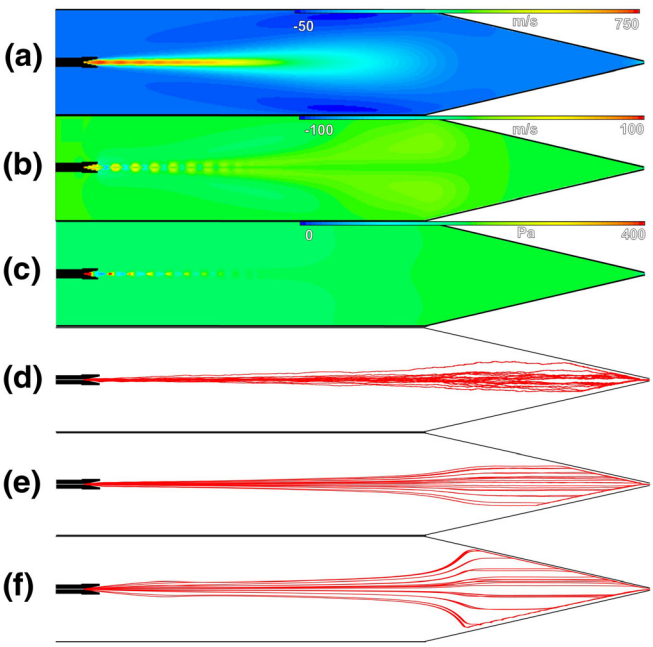

Figure 4. Gas flow and trajectories for interface 3: sealed ion funnel with virtual jet disruptor. Gas flow simulations performed using the Navier-Stokes solver Star-CCM+. (**a**) Axial velocity, (**b**) radial velocity, and (**c**) pressure. Twenty representative ion trajectories of 1000 performed for each mass are shown for (**d**) 1 kDa, (**e**) 1 MDa, and (**f**) 1 GDa

along the entire funnel. Lowering this gradient any further does not decrease the excess ion energy, as this is primarily set by the gas flow through the exit aperture.

Sample ion trajectories are shown in Figure 4d–f. As the ions encounter the nearly static background gas towards the latter portion of the funnel, the ion radial distribution expands, but the ions are now confined and focused by the funnel. Near 100% transmission was achieved for the entire mass range studied (see Figure 2a). Figure 2b shows that low excess kinetic energies were achieved for ion masses of 1 MDa and below. However, for masses greater than 10 MDa, the excess kinetic energy is higher than with interface 2. This demonstrates that it is primarily the gas flow out of the aperture that sets the kinetic energy with this interface [24]. Heavier ions have larger collisional cross sections and thus undergo more collisions with the gas flowing out of the aperture.

The results for interface 3 show that the problem with the transmission of the off-axis high-mass ions has been fixed with the funnel geometry. However, the exit aperture of the funnel caused problems. To avoid ion traps, it was necessary to increase the diameter of the aperture, which resulted in a large mass flow rate that accelerated the ions and led to large excess kinetic energies for the high-mass ions. The carpet can have a small exit aperture, but the problem with the carpet is that it struggles to transmit ions that are a long way off-axis. To transmit these ions, it was necessary to use high-voltage gradients on the carpet and this contributed to the ions' excess kinetic energy. Thus, it occurred to us that a combination of a funnel and carpet may capture favorable features from both types of interface: a funnel to focus ions with a large radial extent and a carpet with a small aperture to transmit them.

Interface 4: FUNPET with Virtual Jet Disruptor

The last 2.159 cm of the ion funnel of interface 3 was removed, leaving behind a 6.35-mm diameter aperture. This diameter matched the 6.35-mm diameter ion carpet which was placed 1.27 mm from the last electrode of the ion funnel. The gap is sealed in the gas flow simulations to ensure adequate pressure buildup. The ion carpet had the same basic parameters as the one used in interface 2 including a 1.016-mm diameter aperture. In addition, because the ion funnel aperture is much larger than in interface 3, axial trapping is not a concern and thus the electrode spacing requirements are relaxed. Therefore, a 2.54-mm electrode pitch was used instead of the 1.27-mm electrode pitch used in interface 3.

The axial (Figure 5a) and radial (Figure 5b) velocities for the FUNPET device closely resemble that of the ion funnel device, with the jet being stopped ~ 27 cm away from the capillary exit. The pressure buildup in the FUNPET device is approximately 1 Pa greater than interface 3, but the smaller aperture associated with the carpet leads to a mass flow rate exiting through the FUNPET aperture of 1.94×10^{-8} kg/s, which is much lower than in interfaces 2 and 3.

For interface 4, it was possible to employ a lower drift gradient than used for interface 3. The first 31 cm of the ion funnel had a constant 5-V/cm drift field, the last 4.5 cm had a constant 1-V/cm drift field, and the intervening 4 cm dropped linearly from 5 to 1 V/cm. Also, the ion carpet gradient was decreased to just 4% of the gradient used in interface 1, while still providing high ion transmission. The ion trajectories shown in Figure 5d–f are similar to those for interface 3.

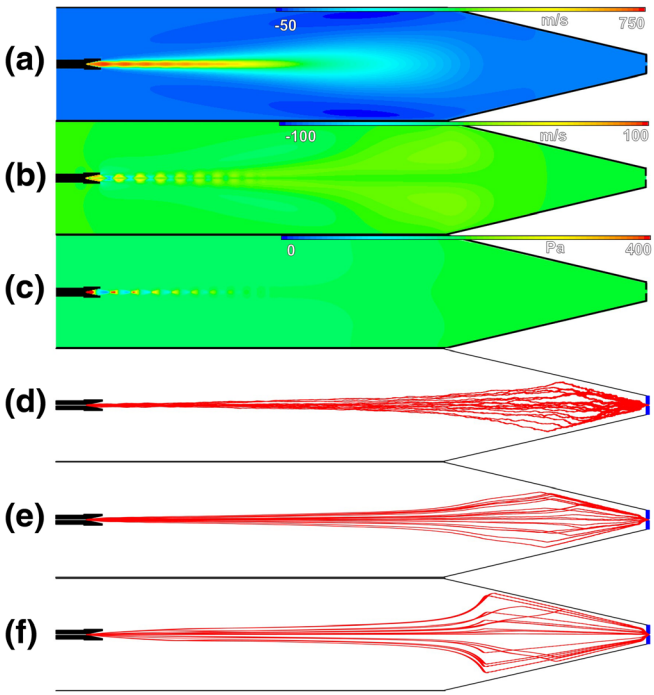

Figure 5. Gas flow and trajectories for interface 4: FUNPET with virtual jet disruptor. Gas flow simulations performed using the Navier-Stokes solver Star-CCM+. (**a**) Axial velocity, (**b**) radial velocity, and (**c**) pressure. Twenty representative ion trajectories of 1000 performed for each mass are shown for (**d**) 1 kDa, (**e**) 1 MDa, and (**f**) 1 GDa

The transmission and excess kinetic energies shown in Figure 2 demonstrate that this is the best performing interface examined here. Nearly 100% transmission was achieved across the entire mass range, with only 1% of the 1-kDa ions crashing out on the surface of the ion carpet due to diffusion. In addition, the FUNPET provided the lowest excess kinetic energies. While the three lightest masses have approximately the same excess kinetic energy as they did with interface 3, the heavier ions have much less excess kinetic energy. This again emphasizes how the heavier ions are more strongly affected by the gas flow. The FUNPET interface had the lowest mass flow rate and the lowest excess kinetic energies. Significantly, the FUNPET transmits 100% of ions in the range of 10 kDa to 1 GDa with the same voltages and RF frequencies. This is a very broad mass range to be examined simultaneously and simplifies the optimization of the interface.

Experimental Methods

The FUNPET was built and installed on a home-built charge detection mass spectrometer similar to that described

previously [36–40]. We decided the best way to construct the FUNPET was to use a flexible printed circuit board (PCB) for the ion funnel component (Figure 6a). The flexible PCB provides ease of assembly and maintenance, similar to that obtained with the rigid PCB ion carpet (Figure 6b). Because of the modest vacuum requirements for the FUNPET, a 3D printed ABS plastic structure is used to support the flexible PCB (Figure 6c). The support structure locates on the flange that mounts the ion carpet PCB.

Ions were generated using a chip-based nano-electrospray source (Advion Triversa NanoMate) and entered the FUNPET through a heated metal capillary (10-cm long, 0.381-mm ID) equipped with a diverging nozzle identical to that used in the simulations (1-cm long diverging from 0.75-mm ID to 5-mm ID). After the FUNPET, ions were confined by an RF hexapole, followed by an RF quadrupole. Ions exiting the quadrupole were focused by an einzel lens and transmitted through two pairs of ion beam deflectors into a dual hemispherical deflection analyzer (HDA). The HDA was set to transmit a narrow band of kinetic energies centered on 130 eV/z. After exiting the HDA, ions are focused into an electrostatic linear ion trap where they oscillate back and forth through a detector tube. All ions were trapped for 100 ms. A charge-sensitive amplifier detects the induced charge that results from the oscillating ion. The resulting signal is amplified, digitized, analyzed using fast Fourier transforms. The oscillation frequency provides the m/z and the magnitude of the Fourier transform provides the charge. The mass of each ion is determined from the product of the m/z and charge. Many mass measurements are performed and the results binned to give the mass distribution.

Measurements were performed with hepatitis B virus (HBV) capsid, bacteriophage P22 procapsid, and amino functionalized polystyrene beads (0.05 μm, Bangs Laboratories Inc.; 0.1-μm Polybead®, Polysciences, Inc.) The HBV capsid was assembled from truncated core protein (Cp149) in sodium chloride (300 mM) and transferred into ammonium acetate (100 mM) by size-exclusion chromatography (SEC) (BIO-RAD Micro Bio-SpinTM 30). The HBV capsid is expected to have a peak at ~4 MDa due to the $T = 4$ capsid and a small peak at ~3 MDa due to the $T = 3$ capsid [40]. P22 procapsid was transferred into 100 mM ammonium acetate by SEC. The procapsid is expected to have a peak at around 20 MDa [39]. The 0.05-μm functionalized polystyrene beads were diluted ten-fold with water, and the 0.1-μm functionalized polystyrene beads were run as received.

Experimental Results

Testing the Performance of the Virtual Jet Disruptor

The FUNPET's ability to transmit a broad mass range is attributed to the disruption of the gas jet by the virtual jet disruptor. This was realized in the simulations for a capillary with a 0.381-mm ID. To test whether the jet was disrupted as indicated by the simulations, we monitored the pressure in the second differentially pumped region (i.e., the region immediately after the FUNPET) as the pressure in the first region was increased by adding gas through a leak valve. The black points in Figure 7 show the pressure in the second differentially pumped region plotted against the pressure in the chamber housing the FUNPET. The point closest to the origin is a measurement with no gas flow added to the FUNPET chamber (i.e., the only gas flow is through the capillary). As the pressure in the FUNPET region is increased, the pressure in the second differentially pumped region increases linearly. This is the behavior expected for a disrupted jet that does not extend to the FUNPET exit aperture.

To illustrate the behavior of a jet that is not disrupted, we increased the ID of the capillary to 1.27 mm keeping the length at 10 cm. The mass flow rate for this diameter, calculated using the Wutz/Adams turbulent model [30], is 2.95×10^{-4} kg/s, 26 times that of the 0.381-mm ID capillary. Simulations with this mass flow rate indicated that the jet will not be stopped by the pressure build-up due to the gas flow through the capillary alone. The results for the larger capillary are represented by the red points in Figure 6. Again, the point closest to the origin is without gas added to the FUNPET chamber. The pressure in the second differentially pumped region is much higher with the 1.27-mm ID capillary than with the 0.381-mm ID capillary. This suggests that the jet for the 1.27-mm DIA capillary is not being stopped before the end of the FUNPET. As gas is added to the FUNPET chamber, the pressure in the second differentially pumped region starts to increase, but then undergoes a sudden drop between 250 and 350 Pa in the FUNPET chamber. As the pressure in the FUNPET chamber is increased further, the pressure in the second differentially pumped chamber increases and gradually approaches the values for the 0.381 ID capillary. The sudden drop in pressure between 250 and 350 Pa in the FUNPET chamber is attributed to the background gas disrupting the gas jet.

These experiments show that with a capillary at the design value of 0.381 mm, the jet is disrupted by a virtual jet disruptor without the addition of extra gas to increase the background pressure. With a much larger capillary (1.27-mm ID), the drift region is too short to disrupt the jet. The jet can be disrupted by adding gas to the FUNPET chamber to increase the background pressure. However, with the much higher pressure in the FUNPET, the gas flow into the second differentially pumped region is much higher and this will cause the excess kinetic energy of the heavier ions to increase significantly.

Measurements of the ion signal transmitted by the FUNPET as a function of pressure in the FUNPET region are given in Supplementary Figure S3. In these experiments, the ions were detected by CDMS. Thus, the ions must not only be transmitted through the electrospray interface, but they must have low excess kinetic energy so that they can be transmitted through the HDA. Results are shown for capillary IDs of 0.381 mm and 1.27 mm. At low pressure, the transmitted signal is low for the 0.381-mm capillary because the ions are not thermalized even though the virtual jet disruptor stops the jet. According to Figure 7, the jet is stopped for the 1.27-mm capillary with a pressure of around 350 Pa in the FUNPET region, but the ion

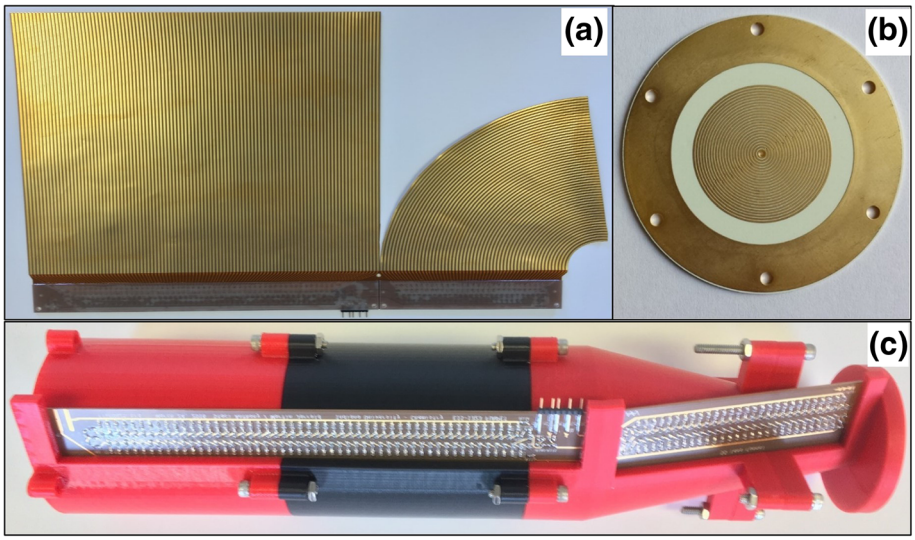

Figure 6. The FUNPET interface assembly. (**a**) The flexible PCB used for the ion funnel portion of the FUNPET. (**b**) The PCB ion carpet. (**c**) The 3D printed FUNPET scaffold that houses the flexible printed circuit board and mounts to the ion carpet

signal does not reach its maximum value until the pressure is 450 Pa because a higher pressure is needed to thermalize the ions than to stop the jet. Above 450 Pa, the signal drops off because a higher drift field is needed to transmit the ions before they are caught in the counter flow. Increasing the drift field shifts the high-pressure drop-off in the signal to higher pressures.

CDMS Spectra Measured for Large Ions

Figure 8 shows CDMS spectra measured for four representative analytes. The CDMS spectrum for HBV (Figure 8a) shows an intense peak at ~4.0 MDa due to the $T=4$ capsid with 120 capsid protein dimers and a smaller peak at ~3.0 MDa due to the $T=3$ capsid. Some kinetically trapped late-stage assembly intermediates are evident between the peaks due to the $T=3$ and $T=4$ capsids [32]. There is also a peak at low mass due to the HBV capsid protein dimer and small oligomers. Figure 8b shows the spectrum measured for the P22 procapsid. The main peak is at 21.1 MDa. The mass of the P22 procapsid is not well defined because it depends on the number of scaffolding proteins that remain inside. However, 21.1 MDa is within the expected range. The P22 procapsid spectrum contains 12,872 ions and took only one hour to collect. Information on the average charge and average *m*/*z* for these samples is given in Supplementary Table 1.

To test the breadth of the mass range transmitted by the FUNPET, CDMS spectra were measured for 0.05-μm and 0.1-μm amino functionalized polystyrene beads (see Figure 8c, d). Both samples contained synthesis byproducts and micelles that were removed from the spectra by filtering out low *m*/*z* values. For the 0.05-μm polystyrene beads, all ions with *m*/*z* values < 100 kDa were omitted, and for the 0.1-μm beads, all ions with *m*/*z* values < 200 kDa were omitted. For the 0.05-μm beads (Figure 8c), the main peak is centered at 28 MDa which corresponds to a diameter of 0.044 μm. This is somewhat smaller than the expected diameter but within the expected tolerance for bead synthesis. For the 0.1-μm polystyrene beads (Figure 8d), the main peak is centered on around 350 MDa, which corresponds closely to the expected diameter. Information on the average charge and average *m*/*z* for these samples is given in Supplementary Table 1.

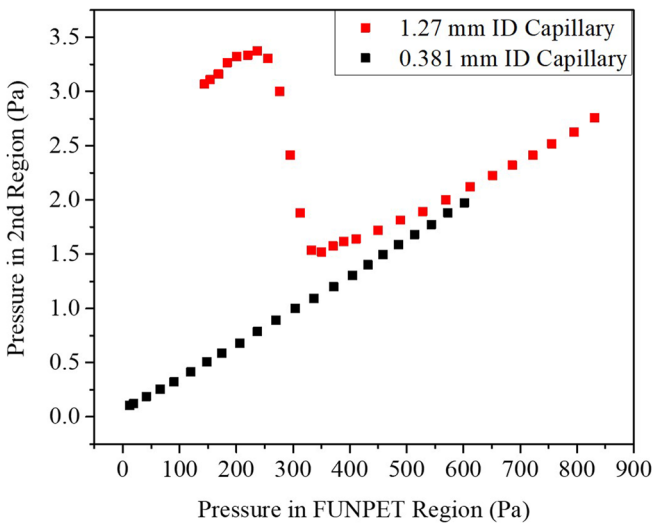

Figure 7. Pressure in the second differentially pumped region plotted against pressure in the FUNPET chamber. The black points were measured with a 0.381-mm ID capillary, and a 1.27-mm ID capillary was used for the red points. In both cases, the point closest to the origin was recorded with just the capillary open to ambient pressure. For the points at higher pressure in the plot, gas was added to the FUNPET chamber through a leak valve. The dip in the pressure for the 1.27-mm ID capillary at 250–350 Pa results from the jet being stopped by the ambient gas flow. The absence of a similar dip for the 0.381-mm ID capillary indicates that the virtual jet disruptor (pressure buildup and counter flow) is stopping the jet in agreement with the predictions of the simulations

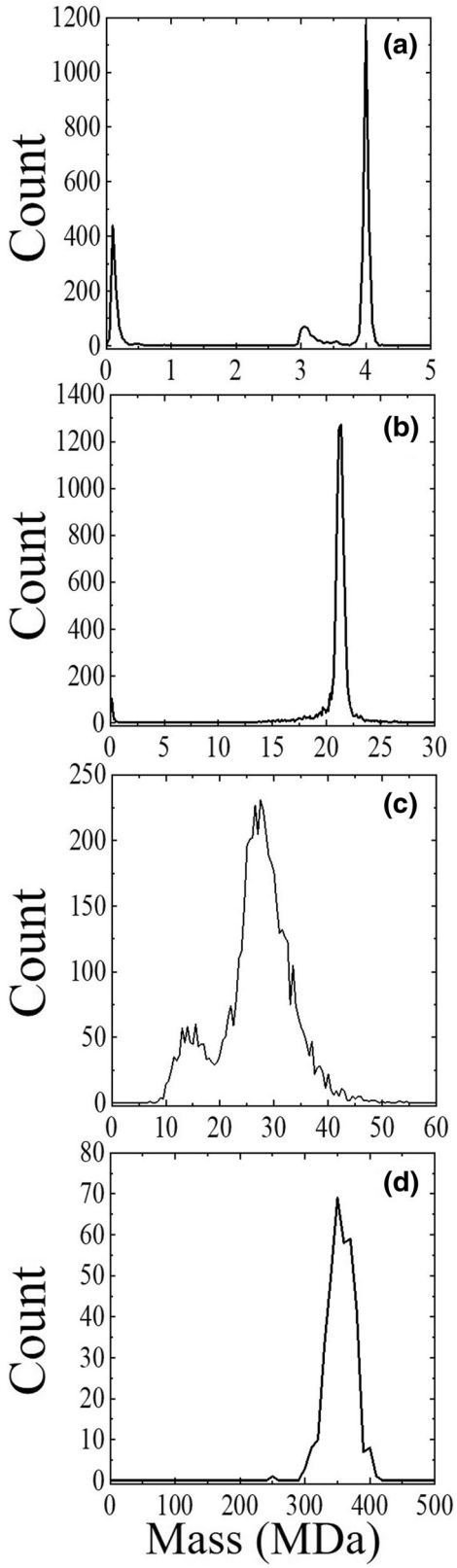

Figure 8.. CDMS spectra measured with the FUNPET interface. (**a**) HBV capsid (0.05-MDa bins; 3825 total ions), (**b**) P22 procapsid (0.1-MDa bins; 12,872 total ions), (**c**) 0.05-μm amino functionalized polystyrene beads with m/z > 100,000 Da (0.5-MDa bins; 5239 total ions), and (**d**) 0.1-μm amino functionalized polystyrene beads with m/z > 200,000 Da (10-MDa bins; 348 total ions)

Compared to the electrospray interface on our prototype instrument, the FUNPET has a higher transmission efficiency and it is much more effective at transmitting high-mass ions. The best way to compare the performance of the interface with the simulations would be to measure the transmission efficiency as a function of m/z (as shown for the simulations in Figure 2). To determine the transmission efficiency, it is necessary to measure the ion current entering the FUNPET and to compare it with the ion current exiting through the carpet aperture. Ideally, this measurement would be performed for ions with a known m/z. However, the ion current entering the FUNPET through the capillary includes many low m/z ions from the solvent that the FUNPET interface will not transmit efficiently. These low m/z ions could contribute to noise if they reached the detector and could contribute to space charge effects in the FUNPET, and so it is desirable to discriminate against them. Because the low m/z ions make up a large fraction of the ions that enter the FUNPET, a direct measurement of the transmission efficiency is not feasible. Finally, it is worth mentioning that the transmission efficiency is not the only important performance metric; it is also important that ions leave the interface with low excess kinetic energy.

Conclusions

A new ion trajectory program that incorporates diffusion, acceleration due to RF and DC fields, acceleration due to drag resulting from gas flow, and gravity has been used to develop an electrospray interface that transmits ions with a broad distribution of masses.

The simulations show that a physical jet disruptor successfully stops the gas jet from the capillary inlet. However, high-mass ions crash out on the surface of the jet disruptor. To overcome this problem, we developed a virtual jet disruptor where the drift region is sealed and the resulting pressure buildup and gas counter flow disrupt the gas jet. An ion carpet interface was found to have low transmission for ions that are far off-axis, reducing the transmission of high-mass ions. An ion funnel can focus ions that are far off-axis towards the exit aperture; however, the exit aperture needed to be relatively large to avoid ion traps. The large exit aperture led to large excess kinetic energies for high-mass ions. The best solution was found by coupling the favorable features of an ion funnel and an ion carpet. In the FUNPET, the ions that are far off-axis are focused by the funnel, but the exit aperture of the funnel is replaced by an ion carpet. The ion carpet focusses exiting ions through a much smaller aperture than could be used with the traditional ion funnel. The small aperture reduces the gas load on the second chamber and minimizes the acceleration of high-mass ions from the flow passing through the aperture. The FUNPET interface was constructed easily and inexpensively from a flexible printed circuit board supported by a 3D printed ABS plastic frame. It has been used for a number of months with a wide variety of samples including proteins and peptides, virus capsids, gene therapy products, micelles, and polystyrene, silica, and metal nanoparticles. We have noticed that there

is some degradation of performance after more than a month of daily use. This was traced to the buildup of a thin film on the carpet, and it was easily removed by gentle wiping with a Kimwipe.

Funding Information

This material is based upon work supported by the National Science Foundation under Grant Number CHE–1531823.

References

1. Doussineau, T., Paletto, P., Dugourd, P., Antoine, R.: Multiphoton dissociation of electrosprayed megadalton-sized DNA ions in a charge-detection mass spectrometer. J. Am. Soc. Mass Spectrom. **26**, 7–13 (2015)
2. van Berkel, W.J.H., van den Huevel, R.H.H., Versluis, C., Heck, A.J.R.: Detection of intact megadalton protein assemblies of vanillyl-alcohol oxidase by mass spectrometry. Protein Sci. **9**, 435–439 (2000)
3. Keifer, D.Z., Motwani, T., Teschke, C.M., Jarrold, M.F.: Measurement of the accurate mass of a 50 MDa infectious virus. Rapid Commun. Mass Spectrom. **30**, 1957–1962 (2016)
4. Scoles, G.: Atomic and molecular beam methods. Oxford University Press, Oxford (1988)
5. Kelly, R.T., Tolmachev, A.V., Page, J.S., Tang, K., Smith, R.D.: The ion funnel: theory, implementations, and applications. Mass Spectrom. Rev. **29**, 294–312 (2010)
6. Wada, M., Ishida, Y., Nakamura, T., Yamazaki, Y., Kambara, T., Ohyama, H., Kanai, Y., Kojima, T.M., Nakai, Y., Oshima, N., Yoshida, A., Kubo, T., Matsuo, Y., Fukuyama, Y., Okada, K., Sonoda, T., Ohtani, S., Noda, K., Kawakami, H., Katayama, I.: Slow-RI beams from projectile fragment separators. Nucl. Instrum. Methods Phys. Res. Sect. B. **204**, 570–581 (2003)
7. Anthony, S.N., Shinholt, D.L., Jarrold, M.F.: A simple electrospray interface based on a DC ion carpet. Int. J. Mass Spectrom. **371**, 1–7 (2014)
8. Shaffer, S.A., Tang, K., Anderson, G.A., Prior, D.C., Udseth, H.R., Smith, R.D.: A novel ion funnel for focusing ions at elevated pressure using electrospray ionization mass spectrometry. Rapid Commun. Mass Spectrom. **70**, 4111–4119 (1997)
9. Shaffer, S.A., Tolmachev, A., Prior, D.C., Anderson, G.A., Udseth, H.R., Smith, R.D.: Characterization of a new electrodynamic ion funnel interface for electrospray ionization mass spectrometry. Anal. Chem. **71**, 2957–2964 (1999)
10. Kim, T., Tang, K., Udseth, H.R., Smith, R.D.: A multicapillary inlet jet disruption electrodynamic ion funnel interface for improved sensitivity using atmospheric pressure ion sources. Anal. Chem. **73**, 4162–4170 (2001)
11. Tridas, E., Anthony, J.M., Guldiken, R., Schlaf, R.: Enhanced simulation of an RF ion funnel including gas turbulence. J. Mass Spectrom. **50**, 206–211 (2015)
12. Tridas, E.M., Allemang, C., Mast, F., Anthony, J.M., Schlaf, R.: High transmission 3D printed flex-PCB-based ion funnel. J. Mass Spectrom. **50**, 938–943 (2015)
13. Naimi, S., Nakamura, S., Ito, Y., Mita, H., Okada, K., Ozawa, A., Schury, P., Sonoda, T., Takamine, A., Wada, M., Wollnik, H.: An RF-carpet electrospray ion source to provide isobaric mass calibrants for trans-uranium elements. Int. J. Mass Spectrom. **337**, 24–28 (2013)
14. Manura, D.J., Dahl, D.A.: SIMION Version 8.0/8.1 User Manual. Scientific Instrument Services, Ringoes (2011)
15. Appelhans, A.D., Dahl, D.A.: SIMION ion optics simulations at atmospheric pressure. Int. J. Mass Spectrom. **244**, 1–14 (2005)
16. Tolmachev, A.V., Kim, T., Udseth, H.R., Smith, R.D., Bailey, T.H., Futrell, J.H.: Simulation-based optimization of the electrodynamic ion funnel for high sensitivity electrospray ionization mass spectrometry. Int. J. Mass Spectrom. **203**, 31–47 (2000)
17. Valentine, S.J., Stokes, S.T., Kurulugama, R.T., Nachtigall, F.M., Clemmer, D.E.: Overtone mobility spectrometry: part 2. Theoretical considerations of resolving power. J. Am. Soc. Mass Spectrom. **20**, 738–750 (2009)
18. Gimelshein, N., Gimelshein, S., Lilly, T., Moskovets, E.: Numerical modeling of ion transport in an ESI-MS system. J. Am. Soc. Mass Spectrom. **25**, 820–831 (2014)
19. Zhou, X., Ouyang, Z.: Flowing gas in mass spectrometer: method characterization and impact on ion processing. Analyst. **139**, 5215–5222 (2014)
20. Gimelshein, S., Lilly, T., Moskovets, E.: Numerical analysis of ion-funnel transmission efficiency in an API-MS system with a continuum/microscopic approach. J. Am. Soc. Mass Spectrom. **26**, 1911–1922 (2015)
21. Prasad, S., Wouters, E.R., Dunyach, J.J.: Advancement of atmospheric-vacuum interfaces for mass spectrometers with a focus on increasing gas throughput for improving sensitivity. Anal. Chem. **87**, 8234–8241 (2015)
22. Brunner, T., Fudenberg, D., Varentsov, V., Sabourov, A., Gratta, G., Dilling, J., DeVoe, R., Sinclair, D., Fairbank, W., Albert, J.B., Auty, D.J., Barbeau, P.S., Beck, D., Benitez-Medina, C., Breidenbach, M., Cao, G.F., Chambers, C., Cleveland, B., Coon, M., Craycraft, A., Daniels, T., Daugherty, S.J., Didberidze, T., Dolinski, M.J., Dunford, M., Fabris, L., Farine, J., Feldmeier, W., Fierlinger, P., Gornea, R., Graham, K., Heffner, M., Hughes, M., Jewell, M., Jiang, X.S., Johnson, T.N., Johnston, S., Karelin, A., Kaufman, L.J., Killick, R., Koffas, T., Kravitz, S., Krücken, R., Kuchenkov, A., Kumar, K.S., Leonard, D.S., Leonard, F., Licciardi, C., Lin, Y.H., Ling, J., MacLellan, R., Marino, M.G., Mong, B., Moore, D., Odian, A., Ostrovskiy, I., Ouellet, C., Piepke, A., Pocar, A., Retiere, F., Rowson, P.C., Rozo, M.P., Schubert, A., Smith, E., Stekhanov, V., Tarka, M., Tolba, T., Tosi, D., Twelker, K., Vuilleumier, J.L., Walton, J., Walton, T., Weber, M., Wen, L.J., Wichoski, U., Yang, L., Yen, Y.R.: An RF-only ion-funnel for extraction from high-pressure gases. Int. J. Mass Spectrom. **379**, 110–120 (2015)
23. Zhou, X., Ouyang, Z.: Following the ions through a mass spectrometer with atmospheric pressure interface: simulation of complete ion trajectories from ion source to mass analyzer. Anal. Chem. **88**, 7033–7040 (2016)
24. Wang, X., Chen, H., Lee, J., Reilly, P.T.A.: Increasing the trapping mass range to $m/z = 10^9$ - a major step toward high resolution mass analysis of intact RNA, DNA and viruses. Int. J. Mass Spectrom. **328-329**, 28–35 (2012)
25. CD-Adapco Star-CCM+ User Guide. CD-Adapco (2015)
26. Bird, G. A.: The DSMC method, Version 1.2. http://www.gab.com.au (2013)
27. Luria, K., Christen, W., Even, U.: Generation and propagation of intense supersonic beams. J. Phys. Chem. A. **115**, 7362–7367 (2011)
28. Krutchinsky, A.N., Padovan, J.C., Cohen, H., Chait, B.T.: Maximizing ion transmission from atmospheric pressure into the vacuum of mass spectrometers with a novel electrospray interface. J. Am. Soc. Mass Spectrom. **26**, 649–658 (2015)
29. Krutchinsky, A.N., Padovan, J.C., Cohen, H., Chait, B.T.: Optimizing electrospray interfaces using slowly diverging conical duct (ConDuct) electrodes. J. Am. Soc. Mass Spectrom. **26**, 659–667 (2015)
30. Wißdorf, W., Müller, D., Brachthäuser, Y., Langner, M., Derpmann, V., Klopotowski, S., Polaczek, C., Kersten, H., Brockmann, K., Benter, T.: Gas flow dynamics in inlet capillaries: evidence for non laminar conditions. J. Am. Soc. Mass Spectrom. **27**, 1550–1563 (2016)
31. Langevin, P.: Sur la theórie du mouvement Brownien. C.R. Acad. Sci. (Paris). 146, 530-533 (1908), English Translation. Am. J. Phys. **65**, 1079–1081 (1997)
32. Sivak, D.A., Chodera, J.D., Crooks, G.E.: Time step rescaling recovers continuous-time dynamical properties for discrete-time Langevin integration of nonequilibrium systems. J. Phys. Chem. B. **118**, 6466–6474 (2014)
33. Mason, E.A., McDaniel, E.W.: Transport properties of ions in gases. Wiley, New York (1988)
34. Mason, E.A., Schamp, H.W.: Mobility of gaseous ions in weak electric fields. Ann. Phys. **4**, 233–270 (1958)
35. Rayleigh, L.: On the equilibrium of liquid conducting masses charged with electricity. Philos. Mag. **14**, 184–186 (1882)
36. Contino, N.C., Jarrold, M.F.: Charge detection mass spectrometry for single ions with a limit of detection of 30 charges. Int. J. Mass Spectrom. **345-347**, 153–159 (2013)

37. Contino, N.C., Pierson, E.E., Keifer, D.Z., Jarrold, M.F.: Charge detection mass spectrometry with resolved charge states. J. Am. Soc. Mass Spectrom. **24**, 101–108 (2013)
38. Pierson, E.E., Contino, N.C., Keifer, D.Z., Jarrold, M.F.: Charge detection mass spectrometry for single ions with an uncertainty in the charge measurement of 0.65 e. J. Am. Soc. Mass Spectrom. **26**, 1213–1220 (2015)
39. Keifer, D.Z., Pierson, E.E., Hogan, J.A., Bedwell, G.J., Prevelige, P.E., Jarrold, M.F.: Charge detection mass spectrometry of bacteriophage P22 procapsid distributions above 20 MDa. Rapid Commun. Mass Spectrom. **28**, 483–488 (2014)
40. Pierson, E.E., Keifer, D.Z., Selzer, L., Lee, L.S., Contino, N.C., Wang, J.C.-Y., Zlotnick, A., Jarrold, M.F.: Detection of late intermediates in virus capsid assembly by charge detection mass spectrometry. J. Am. Chem. Soc. **136**, 3536–3541 (2014)